The $\vec{\gamma}\, p \to K^+\Lambda$ and $\vec{\gamma}\, p \to K^+\Sigma^0$ reactions at forward angles with photon energies from 1.5 to 2.4 GeV

M. Sumihama,[1] J. K. Ahn,[2] H. Akimune,[3] Y. Asano,[4] C. Bennhold,[5] W. C. Chang,[6] T. Corthals,[7] S. Daté,[8] H. Ejiri,[8] H. Fujimura,[9] M. Fujiwara,[1,10] M. Guidal,[11] K. Hicks,[12] T. Hotta,[1] K. Imai,[9] T. Ishikawa,[13] T. Iwata,[14] H. Kawai,[15] Z. Y. Kim,[16] K. Kino,[1] H. Kohri,[1] N. Kumagai,[8] S. Makino,[17] T. Mart,[18] T. Matsumura,[1] N. Matsuoka,[1] T. Mibe,[1] M. Miyabe,[9] Y. Miyachi,[19] M. Morita,[1] N. Muramatsu,[1] T. Nakano,[1] M. Niiyama,[9] M. Nomachi,[20] Y. Ohashi,[8] T. Ooba,[15] H. Ohkuma,[8] D. S. Oshuev,[6] C. Rangacharyulu,[21] A. Sakaguchi,[20] T. Sasaki,[9] P. M. Shagin,[22] Y. Shiino,[15] H. Shimizu,[13] Y. Sugaya,[20] H. Toyokawa,[8] A. Wakai,[23] C. W. Wang,[6] S. C. Wang,[6] K. Yonehara,[24] T. Yorita,[8] M. Yosoi,[1] and R. G. T. Zegers[25]
(LEPS Collaboration)

[1]*Research Center for Nuclear Physics, Osaka University, Ibaraki, Osaka 567-0047, Japan*
[2]*Department of Physics, Pusan National University, Busan 609-735, Korea*
[3]*Department of Physics, Konan University, Kobe, Hyogo 658-8501, Japan*
[4]*Synchrotron Radiation Research Center, Japan Atomic Energy Research Institute, Sayo, Hyogo 679-5198, Japan*
[5]*The George Washington University, Washington, D.C., 20052, USA*
[6]*Institute of Physics, Academia Sinica, Taipei, Taiwan 11529, Republic of China*
[7]*Department of Subatomic and Radiation Physics, Gent University, Proeftuinstraat 86, B-9000 Gent, Belgium*
[8]*Japan Synchrotron Radiation Research Institute, Sayo, Hyogo 679-5198, Japan*
[9]*Department of Physics, Kyoto University, Kyoto 606-8502, Japan*
[10]*Kansai Photon Science Institute, Japan Atomic Energy Agency, Kizu, Kyoto 619-215, Japan*
[11]*Institut de Physique, Nucléaire d'Orsay, F-91406 Orsay, France*
[12]*Department of Physics and Astronomy, Ohio University, Athens, Ohio 45701, USA*
[13]*Laboratory of Nuclear Science, Tohoku University, Sendai, Miyagi 982-0826, Japan*
[14]*Department of Physics, Yamagata University, Yamagata 990-8560, Japan*
[15]*Department of Physics, Chiba University, Chiba 263-8522, Japan*
[16]*School of Physics, Seoul National University, Seoul, 151-747, Korea*
[17]*Wakayama Medical College, Wakayama, Wakayama 641-8509, Japan*
[18]*Departemen Fisika, FMIPA, Universitas Indonesia, Depok 16424, Indonesia*
[19]*Department of Physics, Tokyo Institute of Technology, Tokyo 152-8551, Japan*
[20]*Department of Physics, Osaka University, Toyonaka, Osaka 560-0043, Japan*
[21]*Department of Physics and Engineering Physics, University of Saskatchewan, Saskatoon, Saskatchewan, Canada, S7N 5E2*
[22]*School of Physics and Astronomy, University of Minnesota, Minneapolis, Minnesota 55455, USA*
[23]*Akita Research Institute of Brain and Blood Vessels, Akita 010-0874, Japan*
[24]*Illinois Institute of Technology, Chicago, Illinois 60616, USA*
[25]*National Superconducting Cyclotron Laboratory (NSCL), Michigan State University, Michigan 48824-1321, USA*
(Received 21 December 2005; published 30 March 2006)

Differential cross sections and photon-beam asymmetries for the $\vec{\gamma}\, p \to K^+\Lambda$ and $\vec{\gamma}\, p \to K^+\Sigma^0$ reactions have been measured in the photon energy range from 1.5 to 2.4 GeV and in the angular range from $\Theta_{\mathrm{c.m.}} = 0^\circ$ to 60° of the K^+ scattering angle in the center-of-mass system at the SPring-8/LEPS facility. The photon-beam asymmetries for both the reactions have been found to be positive and to increase with the photon energy. The measured differential cross sections agree with the data measured by the CLAS Collaboration at $\cos\Theta_{\mathrm{c.m.}} < 0.9$ within the experimental uncertainties, but the discrepancy with the SAPHIR data for the $K^+\Lambda$ reaction is large at $\cos\Theta_{\mathrm{c.m.}} > 0.9$. In the $K^+\Lambda$ reaction, the resonance-like structure found in the CLAS and SAPHIR data at $W = 1.96$ GeV is confirmed. The differential cross sections at forward angles suggest a strong K-exchange contribution in the t-channel for the $K^+\Lambda$ reaction, but not for the $K^+\Sigma^0$ reaction.

DOI: 10.1103/PhysRevC.73.035214 PACS number(s): 14.20.Gk, 13.60.Le, 25.20.Lj

I. INTRODUCTION

By studying the excited states of baryons, deeper insight can be gained into their structure. The excited spectrum of baryons contains signatures stemming from the constituents at a more fundamental level. Experimental information on nucleon resonances (N^* and Δ^*) has been obtained primarily from the studies of the πN and $N(\gamma, \pi)$ reactions. In spite of valuable information on resonances in pionic channels, a search of intermediate resonances might be limited in these reactions. This problem is addressed by recent calculations in constituent quark models [1,2]. A considerably large number of nucleon resonances are predicted by theoretical calculations compared with those observed in the pionic reactions. The nucleon resonances predicted but not yet found are referred to as missing resonances. Quark-model studies suggest some of these missing resonances may couple to strange channels,

such as $K\Lambda$ and $K\Sigma$ channels [2]. Λ and Σ^0 hyperons have the isospins of 0 and 1, respectively. Accordingly, intermediate states of $K^+\Lambda$ have the isospin $\frac{1}{2}$ (N^* only), whereas intermediate states of $K^+\Sigma^0$ can have the isospins of both $\frac{1}{2}$ and $\frac{3}{2}$ (N^* and Δ^*). It is very interesting to study the $\gamma p \to K^+\Lambda$ and $\gamma p \to K^+\Sigma^0$ reactions to further our understanding of the role that nucleon resonances play in nonpionic reactions.

Measurements of the total cross section for the $\gamma p \to K^+\Lambda$ reaction at ELSA/SAPHIR [3] showed a new resonance-like structure around $W = 1900$ MeV ($E_\gamma = 1.5$ GeV), where W is the total energy in the center-of-momentum system. The resonance-like structure was theoretically studied by connecting with missing resonances, like the $D_{13}(1900)$, which were predicted to couple strongly to the $K\Lambda$ channel [4–7]. These theoretical calculations were performed in a tree-level effective-Lagrangian approach. The well-established resonances $S_{11}(1650)$, $P_{11}(1710)$, and $P_{13}(1720)$ in an s-channel and K^* and K_1 in a t-channel were included [4–7]. There still remains some controversy in the theoretical description of the K^+ photoproduction, because of ambiguities from the choice of the resonances included, their meson-hadron couplings and form factors at hadronic vertices, and the treatment of the nonresonant background term. In particular, it has been found that the extracted resonance couplings are greatly influenced depending on which background model [6,8,9] is chosen. Thus, caution is advised in drawing conclusions on possible resonance structures.

It is important to measure additional observables and obtain accurate experimental data over a wide kinematical range for developing theoretical models and for improving our knowledge of K^+ photoproduction. Cross sections and recoil polarizations have been obtained at JLab/CLAS [10] and SAPHIR [3,11]. The cross section measurements at CLAS [10] suggest that the resonance-like structure near 1900 MeV has more than one component by examining yields at different K^+ scattering angles. Recently, comprehensive measurements for the $\gamma p \to K^+\Lambda$ and $\gamma p \to K^+\Sigma^0$ reactions extending to $E_\gamma = 2.6$ GeV at SAPHIR have been reported [11]. In addition, measurements of the photon beam asymmetry [12] and the transferred polarization in kaon electroproduction [13] help to further define the K^+-photoproduction mechanism.

Furthermore, to calculate the cross sections of hypernuclear electroproduction, it is helpful to know the precise cross sections of the elementary reaction of kaon photoproduction. Therefore an improvement of the experimental data is also quite important from the view point of hypernuclear physics.

The contribution of t-channel meson exchange is expected to become large at forward angles above the resonance region at $E_\gamma > 2$ GeV. Mesons exchanged in kaon photoproduction are K, K^*, K_1, and higher-mass Regge-poles. The dominance of unnatural parity exchange (K and K_1 exchanges) leads to a photon-beam asymmetry equal to -1, whereas natural parity exchange (K^* exchange) leads to a photon-beam asymmetry equal to $+1$ at the limit of $t = 0$ and $s \to \infty$ [14,15]. Therefore, measurements of the photon-beam asymmetries will provide information relevant to t-channel meson exchange.

In the present article, we report photon-beam asymmetries and the differential cross sections for the $\gamma p \to K^+\Lambda$ and $\gamma p \to K^+\Sigma^0$ reactions measured at $E_\gamma = 1.5$–2.4 GeV at the SPring-8/LEPS facility. The photon-beam asymmetries were obtained by using linearly polarized photons. The photon-beam asymmetries, briefly reported in an earlier letter [12], are the first data in the nucleon resonance region. In contrast to the CLAS detector, the LEPS spectrometer at SPring-8 covers forward-scattering angles. The data presented here is thus complementary to the CLAS data set. Because there remains a significant discrepancy between the CLAS and SAPHIR cross-section data especially at forward angles [10], new cross-section data are important for solving this discrepancy.

II. EXPERIMENT

A. LEPS beam line at SPring-8 facility

The experiment was carried out at the Laser-Electron-Photon beam line (LEPS) at the storage ring of the Super Photon ring 8-GeV facility (SPring-8). At the LEPS beam line, a multi-GeV photon beam was produced by backward-Compton scattering of laser light from the circulating 8-GeV electrons.

A schematic view of the LEPS beam line is shown in Fig. 1. The direction and polarization of the laser was tuned

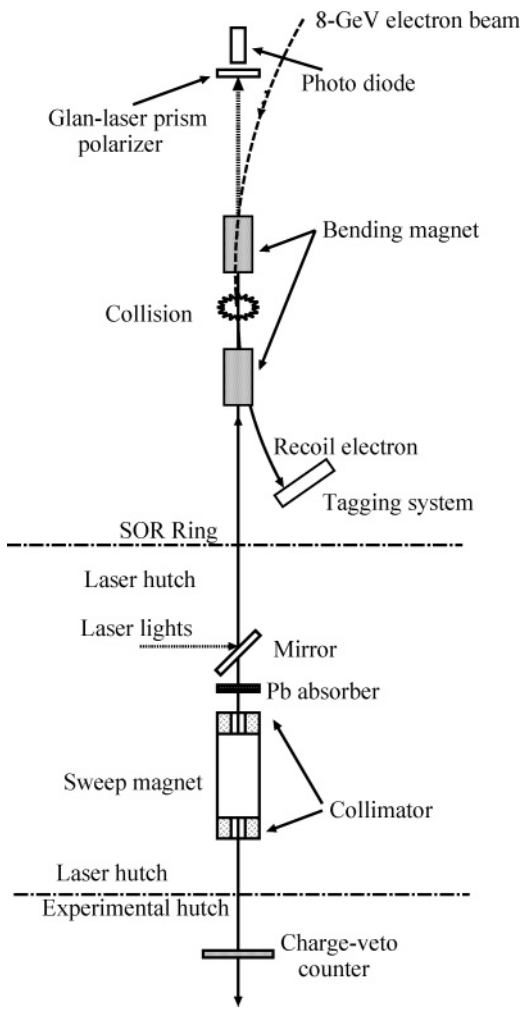

FIG. 1. Schematic view of the LEPS facility at SPring-8.

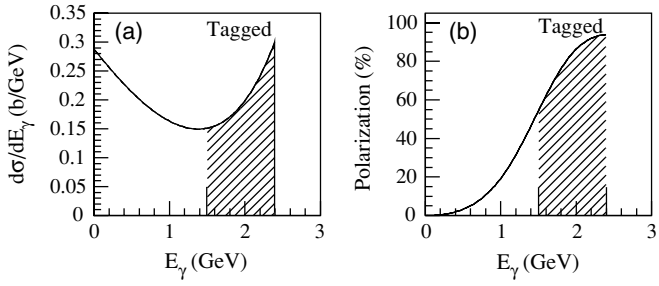

FIG. 2. (a) Intensity distribution and (b) linear polarization of the photon beam as a function of photon energy (E_γ), calculated for the 8-GeV incident electron beam and laser light with a wavelength of 351 nm. The polarization of the laser is assumed to be 100%. The shaded areas correspond to the photon energy region tagged by recoil electrons.

using mirrors and a half-wavelength plate. The laser light was reflected into the beam line and injected in a 7.8-m straight section of the storage ring. The backward-Compton process occurs when laser light collides with the 8-GeV electrons. The photons are scattered backward toward the experimental hutch where a target and a magnetic spectrometer are located.

In the present experiment, an Ar-ion laser was used. Laser light with wavelengths ranging from 333.6 to 363.8 nm was obtained from the ultraviolet multiline mode of operation. Linearly polarized laser light produces linearly polarized GeV energy photons. The polarization of the laser light was measured using a Glan-laser prism polarimeter and a photo diode placed at the end of the straight section. The degree of polarization of the laser light was typically 98%.

Figure 2(a) shows the intensity distribution of photons produced by the backward-Compton process as a function of the photon energy [16]. The maximum energy of the photon beam was 2.4 GeV. The lowest energy of the tagged photon beam (see below) was 1.5 GeV. Figure 2(b) shows the degree of the linear polarization of the photon beam as a function of photon energy [16]. The polarization of the photon beam was 95% at the maximum energy, 2.4 GeV. The polarization drops as the photon energy decreases. However, it is still as high as 55% at 1.5 GeV. The typical photon intensity, integrated from 1.5 GeV to 2.4 GeV, was $5 \times 10^5/s$ with a laser power of 5 W. The size of the photon beam at the target position, which is about 70 m from the collision point in the storage ring, was $\sigma_x = 5$ mm in the horizontal direction and $\sigma_y = 3$ mm in the vertical direction.

The energy of the photon beam was determined by measuring the energy of the recoil electron from Compton scattering with a tagging counter, placed at the exit of the bending magnet next to the straight section (see Fig. 1).

Figure 3 shows the tagging counter, which consists of two layers of scintillator hodoscopes and two layers of silicon strip detectors (SSD). The size of the scintillator was 10 mm high, 8.6 mm wide, and 5 mm thick. The hodoscope consisted of 10 plastic scintillation counters stacked with an overlap of 2.2 mm. The trigger required at least one hit in each layer of the hodoscope. The hodoscopes were used to reject accidental events. After finding a track candidate with two layers of the hodoscope, an associated hit at the SSD was found and the

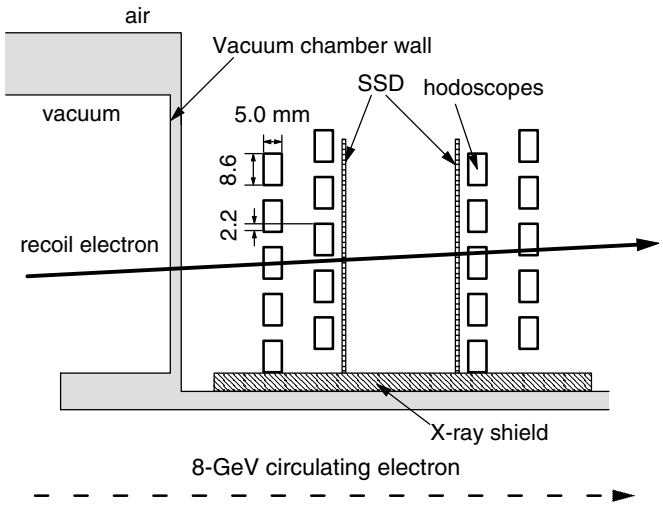

FIG. 3. Schematic top view of the tagging counter.

precise hit position of a recoil electron was measured by the SSD layers with a strip pitch of 0.1 mm. The photon energy coverage of the tagging counter was from 1.5 to 2.4 GeV. The photon energy resolution was 15 MeV in root-mean-square (rms) mainly stemming from the energy and angular spread of the 8-GeV circulating electrons and the uncertainty of the photon-electron interaction point.

An aluminum coated silicon mirror of 0.85 mm thickness reflected the laser light, and a lead sheet of 2 mm thickness was also placed in the beam line. Its purpose was to absorb x rays, thereby protecting the detectors from radiation damage. A part of the photon beam converted to charged particles in these materials. The charged particles were removed by a sweep magnet that consisted of a permanent magnet with a gap of 4.4 cm and a length of 100 cm. The strength of the magnetic field was 0.6 T. Lead beam collimators were placed upstream and downstream of the sweep magnet. The upstream and downstream collimators had holes with a diameter of 20 and 25 mm, respectively. The size of those holes was much larger than the spread of the photon beam. Charged particles produced by the exit windows and the residual gas in the vacuum pipe between the sweep magnet and the target were eliminated using a charge-veto plastic scintillation counter placed just before the target.

B. LEPS spectrometer

The target was liquid hydrogen in a cell with a trapezoid shape made of copper. The length of the target cell was 5 cm in the beam direction and the inner volume was 110 cm^3. The entrance and exit windows of the target cell were made of an Aramid foil of 0.05 mm thickness. The exit aperture was circular in shape with a 35-mm diameter.

The LEPS spectrometer, shown in Fig. 4, was designed to detect charged hadrons produced at forward angles. Figure 5 shows the setup in front of the dipole magnet in more detail. The spectrometer consisted of a start counter (SC), a silica-aerogel Čerenkov counter (AC), a silicon vertex detector (SVTX), a dipole magnet, three multiwire drift chambers

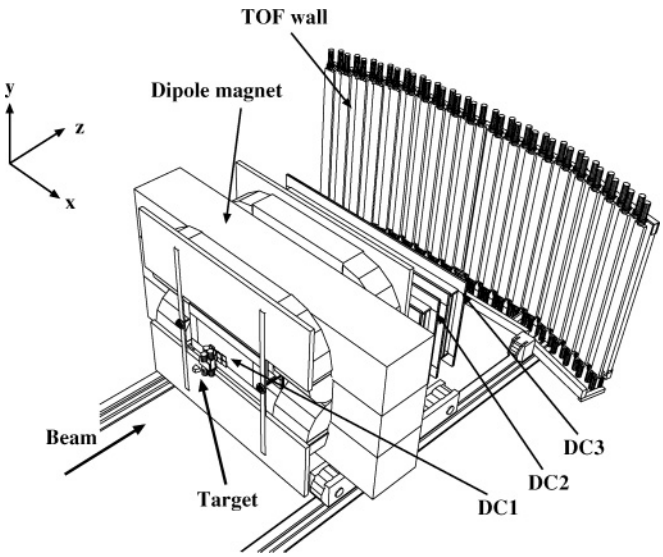

FIG. 4. The LEPS spectrometer.

(DC1, DC2 and DC3), and a time-of-flight (TOF) wall. The field strength of the dipole magnet was 0.7 T at its center. The magnet aperture was 55 cm high and 135 cm wide. The pole length was 60 cm along the beam direction. The angular coverage of the spectrometer was about ± 0.4 rad and ± 0.2 rad in the horizontal and vertical directions, respectively.

Charged particles produced at the target hit the SC, which is 5 mm thick and is located just behind the target. The signal from the SC determined the trigger timing for the data acquisition system. The main background in the measurement of photon induced hadronic reactions is e^+e^- events from pair production. The AC had a 60-mm silica-aerogel radiator with a refractive index of 1.03 and was used to reject e^+e^- events at the trigger level. Gortex sheets were used as a reflector for the light collection. The rejection efficiency for e^+e^- events was higher than 99.9%. The magnetic field of the dipole magnet bent the trajectories of low-momentum positrons and electrons. To prevent radiation hazards, positrons and electrons with momenta below 1 GeV/c were blocked by two lead bars in the dipole magnet. Figure 6 shows the top view of the lead bars. The lead bars with 4 cm height were located in

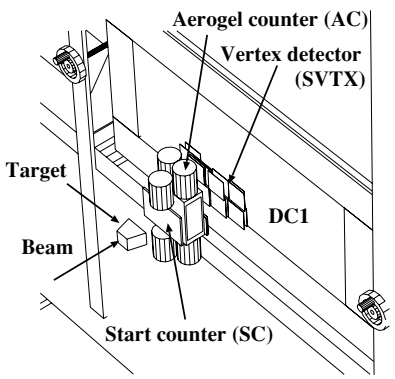

FIG. 5. Detectors upstream of the dipole magnet.

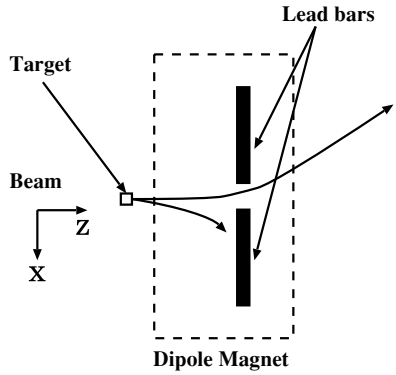

FIG. 6. Schematic top view of the lead bars.

the horizontal plane of the dipole magnet. The area covered by the lead bars corresponded to about 6% of the aperture of the dipole magnet. The positrons and electrons with momenta above 1 GeV/c went through the 15.5-cm gap between the two lead bars and into the beam dump positioned behind the TOF wall.

The silicon vertex detector (SVTX) and three drift chambers were used as tracking devices. SVTX was located behind the AC. By using the silicon detectors, precise vertex positions were obtained. The SVTX consisted of two layers of silicon-strip detectors with a 0.12-mm pitch. One layer was used to measure the position in horizontal direction and the other in the vertical direction. SVTX had a hole of 10×10 mm for the beam. One of drift chambers (DC1) was positioned upstream of the magnet and had 6 layers (3 vertical layers, 2 layers at $+45^\circ$, and 1 layer at -45°). The active area of DC1 was 30 cm high $\times$ 60 cm wide. The other two chambers (DC2 and DC3) were positioned at the downstream of the magnet and had 5 layers: 2 vertical layers, 2 layers at $+30^\circ$, and 1 layer at -30°. The active area was the same for DC2 and DC3, at 80 cm high $\times$ 200 cm wide. The gas mixture used to operate the drift chambers was 70% argon and 30% isobutane. The position resolution of the drift chambers was 200 μm (rms). The average efficiency of each layer was about 99%.

The TOF wall located at the downstream of the DC3 was an array of 40 plastic scintillators. The dimension of each scintillation counter was 12 cm wide, 4 cm thick, and 200 cm high. The counters were placed with an overlap of 1 cm. Photomultiplier (PM) tubes were attached to the top and bottom of the counter. The typical time resolution of the TOF counters was 120 ps.

The event trigger was made by signals from the tagging hodoscopes, the SC and the TOF wall. Signals from the charge-veto counter and the AC were used as vetos. The typical trigger rate was 20 Hz. The dead time of the data acquisition system was about 3%.

Half of the data were taken with vertically polarized photons and the other half with horizontally polarized photons. The polarization was changed about every 6 hr to reduce systematic errors in the measurement of the photon beam asymmetries. The laser polarization was also measured about every 6 hr. The data were accumulated with 2.1×10^{12} photons at the target in total.

III. DATA ANALYSIS

A. Event reconstruction

Momenta of charged particles were determined using information from the vertex detector and the three drift chambers. In the first stage of the tracking process, straight-line tracks were defined separately in the upstream devices (SVTX and DC1) and in the downstream devices (DC2 and DC3/TOF) to determine the hit position from the drift distance and the wire address. After straight-line tracking, track candidates were listed from all possible combinations of the upstream and downstream tracks. The overall track fitting was performed for all the track candidates using the full information of hits. The Kalman filter technique was employed for the track fitting taking into account the effect of the multiple scattering [17]. The trajectory of a charged particle in the inhomogeneous magnetic field of the LEPS magnet was calculated by the Runge-Kutta method. Tracks fitted within a 98% confidence level were accepted for further analysis.

The vertical position in the TOF counter was calculated from the time difference of the TDC signals between the two PM tubes attached to the top and bottom of a counter. The resolution in vertical hit position was 18 mm (σ). The vertical hit position was used to find the correct combination between a track and a TOF hit. The stop signal for the time-of-flight measurement was provided from signals of the TOF counters. The start signal was provided by the RF signal from the 8-GeV electron storage ring where electrons were bunched at 2-ns intervals with a width of 12 ps (rms). The typical flight path of charged particles was 4.2 m. Because the electronics used for recording the RF timing was not working for a part of the experiment, the start counter (SC) was used to provide a start timing instead of the RF signal for two-thirds of the data. The time resolution of the SC was 150 ps, and the TOF resolution was 180 ps.

The particle mass was calculated using the momentum, the path length, and the TOF. Figure 7 shows the momentum versus the square of mass. The mass resolution depends on the momentum, as one can see in the plot. The resolution of kaon mass was 30 (105) MeV/c^2 at the 1 GeV/c (2 GeV/c) momentum.

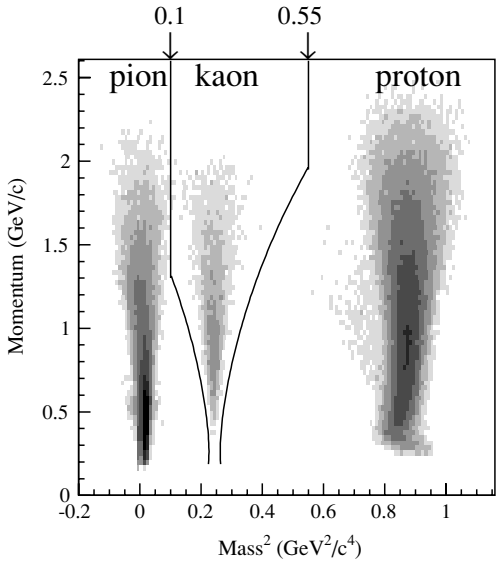

FIG. 7. Two-dimensional scatter plot of momentum vs. mass squared. Cut boundaries (3σ) of the PID selections are displayed.

B. Event selections

To select events from the $\gamma p \to K^+\Lambda$ and $\gamma p \to K^+\Sigma^0$ reactions, we required the following cut conditions: (1) select K^+ particles, (2) remove decay-in-flight kaons, (3) reject accidental e^+e^- events, (4) select reaction vertices in the target, (5) select a recoil electron by Compton scattering and to reject shower and accidental hits in the tagging counter, and (6) select either Λ or Σ^0 production.

The K^+ particles were selected using the known mass and charge. The curves in Fig. 7 indicate the 3σ boundary of the momentum-dependent mass resolution for kaons. The 3σ cut was used to select kaons with an additional condition of $0.1 < \text{mass}^2 < 0.55$ in the overlap region with positive pions and protons at high momenta. Events were purified by selecting events within the 98% confidence level for track fitting. This selection rejected mainly decay-in-flight kaons. The position difference between a track and a TOF hit was also used to reject decay-in-flight kaons. Although most of the accidental e^+e^- events were rejected in the K^+ particle selection, there still remained a contamination of accidental e^+e^- events. Those events were rejected by removing events with particles emitted in the median plane and passing through the gap in the lead bars.

Events produced at the liquid hydrogen target (LH_2) were selected by their calculated vertex position along the photon beam direction (z vertex). Figure 8 shows the z vertex distribution.

The vertex point was defined as the point of the closest approach between a track and the beam axis. The photon beam had a small but finite size and we had no information on the position of a photon at the target on an event-by-event basis. The cut condition to select events produced at the target was

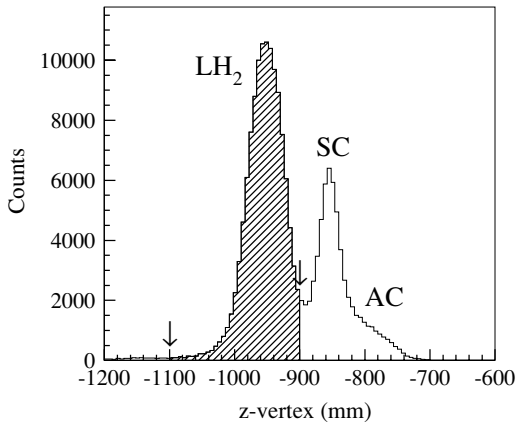

FIG. 8. Distribution of vertex position along the beam direction (z vertex). The liquid hydrogen target (LH_2) and the start counter (SC) positions are easily seen. The shoulder around -800 mm corresponded to the events from the aerogel counter (AC). Cut positions are indicated by the shaded area.

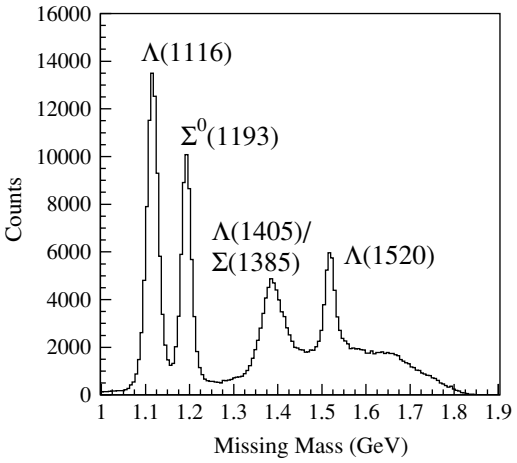

FIG. 9. Missing mass of the $\gamma p \to K^+ X$ reaction. The peaks correspond to the $\Lambda(1116)$, $\Sigma^0(1193)$, and hyperon resonances.

$-1100\,\text{mm} < z$ vertex $< -900\,\text{mm}$. The downstream cut point was tightened to reduce contamination events from the SC.

The number of electron tracks reconstructed in the tagging counter was required to be 1. Electromagnetic shower events or accidental events could make a trigger, but these background events were rejected by requiring one track. After selecting K^+ particles and calculating the photon energy from the hit position of a recoil electron in the tagging counter, the missing mass of the $\gamma p \to K^+ X$ reaction was calculated to identify Λ and Σ^0 particles.

Figure 9 shows the missing mass spectrum of the K^+ photoproduction. Peaks corresponding to Λ and Σ^0 were observed.

The missing mass resolution depends on the K^+ momentum as shown in Fig. 10. The mass resolution of Λ and Σ^0 particles are $\sigma_{\text{mass}} = 17\ \text{MeV}/c^2$ at a 2.0 GeV/c K^+ momentum and $\sigma_{\text{mass}} = 11\ \text{MeV}/c^2$ at a 1.2 GeV/c K^+ momentum. The $2\sigma_{\text{mass}}$ boundaries were used to select Λ and Σ^0 particles.

Table I shows the number of events surviving after the selection cuts. From the total set of 1.8×10^8 triggered events,

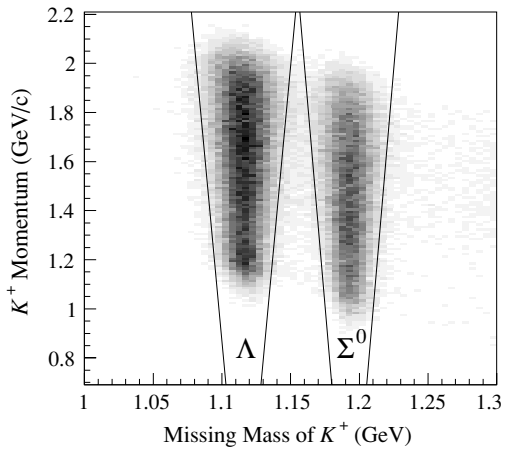

FIG. 10. Two-dimensional scatter plot of momentum vs missing mass of K^+. The solid lines represent missing mass cuts corresponding to 2σ mass deviations from mean values.

TABLE I. The number of events after selection cuts for the beam-polarization asymmetry analysis.

Selection cuts	Events
Triggered events	1.78×10^8
Single track reconstructed	4.23×10^7
K^+ selection	1.67×10^6
K^+ decay-in-flight rejection	1.52×10^6
e^+e^- rejection	9.70×10^5
LH_2 target selection by z vertex	4.52×10^5
One recoil electron in tagger	3.39×10^5
Λ / Σ^0 particles	$7.25 \times 10^4 / 4.89 \times 10^4$

7.3×10^4 and 4.9×10^4 events of the $K^+\Lambda$ and $K^+\Sigma^0$ reactions satisfied all the cut conditions given above.

IV. RESULTS

A. Photon-beam asymmetries

By using both vertically and horizontally polarized photon beams, two sets of data were accumulated to measure the photon-beam asymmetries [12]. The relation between production yields in the two sets of data and the photon-beam asymmetry, Σ, is given as follows:

$$P_\gamma \Sigma \cos 2\Phi = \frac{nN_v - N_h}{nN_v + N_h}, \tag{1}$$

where N_v and N_h are the K^+ photoproduction yields with the vertically and horizontally polarized photons, respectively, and n is the normalization factor for N_v, determined by using the numbers of horizontally polarized photons, n_h, and vertically polarized photons, n_v, at the target as $n = n_h/n_v$. The value of n is 0.923 in the present experimental data. Φ is the K^+ azimuthal angle defined by the angle between the reaction plane and the horizontal plane, and P_γ is the polarization degree of the photon beam.

The Φ dependence of the ratio $(nN_v - N_h)/(nN_v + N_h)$ was fitted with the function $\cos 2\Phi$ as shown in Fig. 11 and the amplitude $P_\gamma \Sigma$ was obtained. After P_γ was calculated, using the photon energy E_γ and the laser polarization shown in Fig. 2(b), the photon beam asymmetry Σ was obtained.

The contamination of positive pions and protons into the K^+ mass region was estimated by extrapolating the Gaussian shaped mass distributions of positive pions and protons into the K^+ region. The contamination rates increased with K^+ momentum because the mass resolution was poor at the higher momenta. The contamination rates of positive pions and protons for the $K^+\Lambda$ at the highest K^+ momentum region were 2.0 and 2.5%, respectively. The contamination rates of positive pions and protons for the $K^+\Sigma^0$ were 3.5 and 5.0% at the highest K^+ momentum region, respectively. Although the contamination rates were small, their contribution caused a nonnegligible shift of the measured photon beam asymmetry. The measured photon beam asymmetry is written as $\Sigma^{\text{meas}}_{K^+} = (1 - C_{\text{bg}})\Sigma_{K^+} + C_{\text{bg}}\Sigma_{\text{bg}}$. The photon-beam asymmetry of the K^+ events, Σ_{K^+}, was obtained by determining the contamination rate, C_{bg}, and the photon-beam asymmetry of the background events, Σ_{bg}. The maximum correction for the

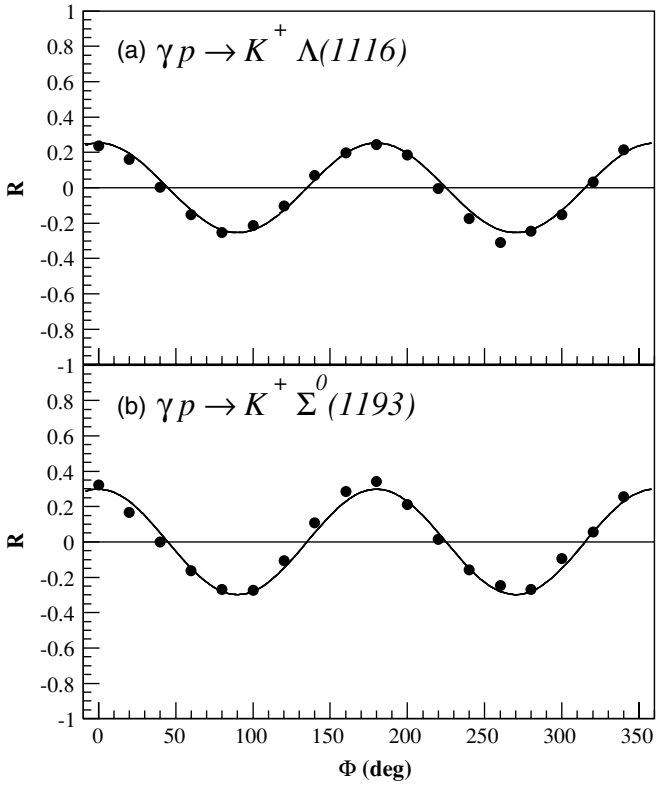

FIG. 11. Azimuthal angle Φ dependence of the ratio $R = (nN_v - N_h)/(nN_v + N_h)$ in Eq. (1) for (a) the $\gamma p \to K^+\Lambda$ reaction and (b) $\gamma p \to K^+\Sigma^0$ reaction integrating over all events. The solid lines are the result of fitting using a function of $\cos 2\Phi$.

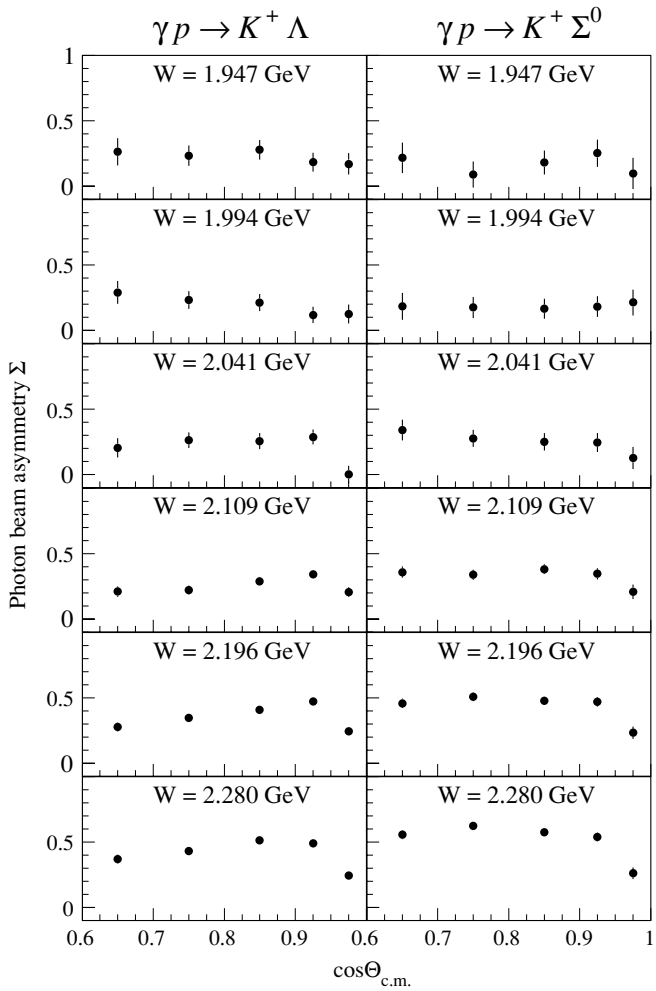

FIG. 12. Photon-beam asymmetries for the $\gamma p \to K^+\Lambda$ (left) and $\gamma p \to K^+\Sigma^0$ (right) reactions as a function of $\cos\Theta_{c.m.}$.

contamination of positive pions and protons was $\delta\Sigma = 0.026$ at $W = 2.28$ GeV ($E_\gamma = 2.3$ GeV). Another correction was made for background from the SC, estimated as a function of the K^+ scattering angle. The contamination rate was lower than 1% at $\cos\Theta_{c.m.} < 0.9$. It was 1.5 and 6.5% for the $K^+\Lambda$ events at $\cos\Theta_{c.m.} = 0.925$ and 0.975, respectively. For the $K^+\Sigma^0$ events, it was 2.5 and 11% at $\cos\Theta_{c.m.} = 0.925$ and 0.975, respectively. The contamination rate for the $K^+\Sigma^0$ reaction was about 2 times higher than that for the $K^+\Lambda$ reaction because $\Sigma^-(1197)$ events, from the $\gamma n \to K^+\Sigma^-$ reaction in carbon from the SC, were also present in the missing mass selection of the Σ^0 events.

Figure 12 shows the experimental results of the photon beam asymmetries as a function of $\cos\Theta_{c.m.}$ for the $K^+\Lambda$ and $K^+\Sigma^0$ reactions in the photon energy range from 1.5 to 2.4 GeV. The errors are statistical only. Systematic uncertainties resulted from (1) the photon-yield normalization factor n, (2) the polarization degree, and (3) the polarization direction of the photon beam. To investigate the accuracy of the normalization factor obtained from the counting rate of the tagging counter, a fitting was performed with a function of $p_1 \cos 2\Phi + p_2$ including an additional offset parameter of p_2. As the result of the fitting, the systematic error for the photon asymmetries was estimated to be $\delta\Sigma = -0.02 \sim +0.06$. The measurement error of the laser polarization was estimated to be $\pm 1.5\%$ ($|\delta\Sigma| < 0.01$). The polarization, P_γ, was calculated by assuming that the wavelength of laser light was 351 nm (which was the most dominant component). The systematic error of P_γ because of the uncertainty of the wavelength, was smaller than 0.1%. The direction of the polarization deviated from 0° and 90° in the cases of horizontal and vertical polarization, respectively. The deviation was 4° at a maximum. The systematic error arising from this deviation was estimated to be smaller than 0.4% ($|\delta\Sigma| < 0.001$).

The signs of the photon-beam asymmetries for both of the $K^+\Lambda$ and $K^+\Sigma^0$ reactions were found to be positive in the measured kinematical region. The positive sign means that K^+ particles are emitted preferentially in the orthogonal direction to the photon polarization. In both reactions the photon-beam asymmetry increases with increasing photon energy and shows an angular distribution flat below $W = 2.0$ GeV. Compared to the $K^+\Lambda$ channel, the photon-beam assymetries for the $K^+\Sigma^0$ channel exhibits a flatter dependence on angle.

The ESRF/GRAAL Collaboration reported the measurements of photon-beam asymmetries for the $K^+\Lambda$ reaction at total energies up to 1.87 GeV ($E_\gamma = 1.4$ GeV) [18]. Their preliminary experimental analysis resulted in a positive sign and a flat angular distribution over all angles at $W = 1.87$ GeV.

The GRAAL data show a good connection to the LEPS data around $W = 1.92$ GeV ($E_\gamma = 1.5$ GeV).

B. Differential cross sections

When the SC was used to provide the time-of-flight start timing, multihit events from a fast proton (from hyperon decay) and a K^+ particle caused a deterioration of the time resolution. This led to an efficiency loss in the particle identification. In the analysis of cross sections, we used only the part of the data with a good quality RF signal.

The data set used in this analysis were accumulated with the same number of photons for the horizontal and vertical polarizations ($n_v = n_h$). Because the $K^+\Lambda$ and $K^+\Sigma^0$ reactions have finite values of the photon-beam asymmetry, the production yield, N_{K^+}, was the average of yields obtained with vertically and horizontally polarized photon beams. Differential cross sections were calculated as follows:

$$\frac{d\sigma}{d\cos\Theta_{\text{c.m.}}} = \frac{(N_{K^+} - N_{\text{BG}})/a}{N_B N_T \Delta\cos\Theta_{\text{c.m.}}}, \tag{2}$$

where a is for the correction of the efficiency of the K^+ selection including the detector acceptance, and N_{BG} is a correction for the contamination of background. N_T is the number of protons inside the target cell and N_B is the number of photons at the target. In this analysis, $\Delta\cos\Theta_{\text{c.m.}}$ was 0.1.

When the target cell was filled with liquid hydrogen, the typical pressure and temperature were 1.05 atm and 20.0 K, respectively, and N_T was 2.37×10^{23} protons/cm^2. The photon number, N_B was obtained by counting the number of hits in hodoscopes of the tagging counter. The efficiency of the hodoscopes and the acceptance of finding a track of a recoil electron were taken into account. The discriminator dead time in electronics, because a high count rate in the hodoscopes, was corrected to obtain the number of photons. The photon beam transmission from the collision point in the storage ring to the target position was measured with a $PbWO_4$ crystal calorimeter. The result of the transmission measurement was consistent with an estimated value from the photon beam loss by material in the LEPS beam line.

The conditions to select the $K^+\Lambda$ and $K^+\Sigma^0$ reaction events are the same as those used in the analysis of the photon-beam asymmetries. Table II shows the number of events that survive after the selection cuts.

TABLE II. The number of events after the selection cuts for the differential cross-section analysis.

Selection cuts	Events
Triggered events	3.68×10^7
Single track reconstructed	7.68×10^6
K^+ selection	2.80×10^5
K^+ decay-in-flight	2.59×10^5
e^+e^- rejection	2.46×10^5
LH_2 target selection by z vertex	1.22×10^5
One recoil electron in Tagger	9.11×10^4
Λ/Σ^0 particles	$2.19 \times 10^4/1.45 \times 10^4$

TABLE III. Acceptance rate with the selection cuts for the $\gamma p \to K^+\Lambda$ reaction obtained by the simulation.

Cuts	$\cos\Theta_{\text{c.m.}}$ range		
	0.9–1.0	0.8–0.9	0.7–0.8
Triggered events	.645	.399	.258
K^+ decay-in-flight rejection	.974	.970	.965
e^+e^- rejection	.954	.995	.992
LH_2 target selection by z vertex	.928	.977	.988
Total	.556	.376	.244

In total, 2.19×10^4 and 1.45×10^4 events for the $K^+\Lambda$ and $K^+\Sigma^0$ reactions, respectively, were used for the differential cross sections.

The acceptance of K^+ particles was estimated by assuming a Gaussian shape of the mass distributions. The acceptance of the K^+ selection was 94% at the highest momenta, as the cut position was set tighter there because of deteriorated mass resolution. The acceptance of selecting K^+ particles and hyperons was corrected by the factor of a in Eq. (2). The amounts of contamination of positive pions and protons in the K^+ event samples were 1.7 and 2.2% for $K^+\Lambda$ and $K^+\Sigma^0$ production, respectively, in the highest K^+ momentum region. The contamination from the SC was the same as that in the photon asymmetry analysis. The contaminations of Σ^0 in the $K^+\Lambda$ sample and Λ in the $K^+\Sigma^0$ sample were smaller than 1%. The contamination from the target windows was estimated to be 4.2%. These backgrounds were subtracted from the yield, N_{K^+}.

The spectrometer acceptance, including the efficiency for track reconstruction, was estimated using a simulation tool based on the GEANT3 package. The acceptance, which depended on the photon energy and the K^+ scattering angle, was calculated for the $K^+\Lambda$ and $K^+\Sigma^0$ reactions. In Table III, the acceptance is listed for the $K^+\Lambda$ reaction with selection cuts at each scattering angle, $\cos\Theta_{\text{c.m.}} = 0.75$, 0.85, and 0.95, integrated over all photon energies. The acceptance for the $K^+\Sigma^0$ reaction is almost the same as that for the $K^+\Lambda$ reaction, because of only small difference of the K^+ momentum.

The vertex resolution was poor at forward scattering angles, which caused a high rejection rate by the z-vertex cut at $\cos\Theta_{\text{c.m.}} = 0.95$. About 56, 38, and 24% of the K^+ events were detected, and the mass was reconstructed, for $\cos\Theta_{\text{c.m.}} =$ 0.95, 0.85 and 0.75, respectively.

Figures 13 and 14 present results of differential cross sections (closed circles) for the $K^+\Lambda$ and $K^+\Sigma^0$ reactions. Differential cross-section data for the $K^+\Lambda$ and $K^+\Sigma^0$ reactions were obtained with good statistics in the W range from 1.92 to 2.32 GeV at $\cos\Theta_{\text{c.m.}} = 0.95$. The systematic uncertainties of the target thickness, because of fluctuations of the temperature and pressure of the liquid hydrogen, is estimated to be 1.0%. The systematic error of the photon number normalization was estimated using the number of protons detected by the LEPS spectrometer. The fluctuation of the photon number was within 1.2%. The measurement error in the transmission of the photon beam was 3.0%. The systematic uncertainty of the aerogel Čerenkov counter (AC)

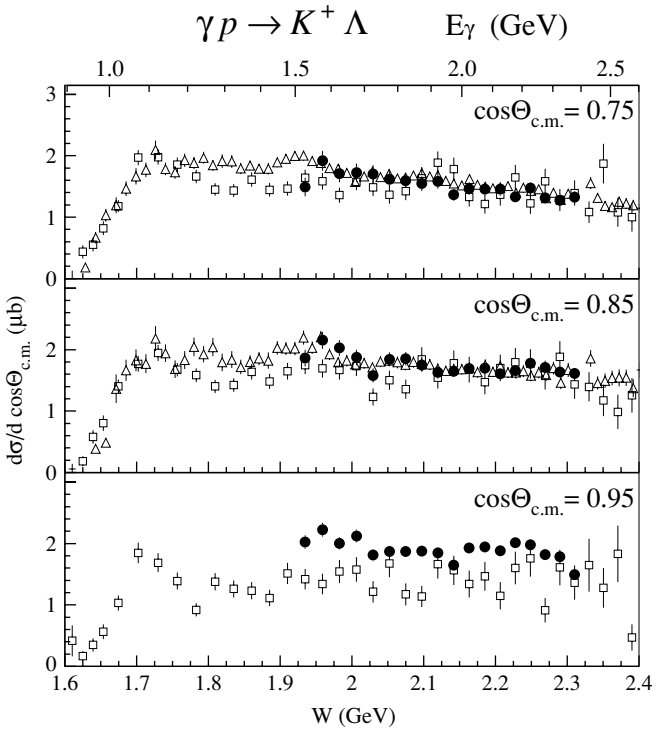

FIG. 13. Energy dependence of differential cross sections for the $\gamma p \to K^+\Lambda$ reaction. The closed circles are the results of the present analysis. The open squares and triangles are the data measured by the SAPHIR [3] and the CLAS [10] Collaborations, respectively. Errors are only because of the statistical one.

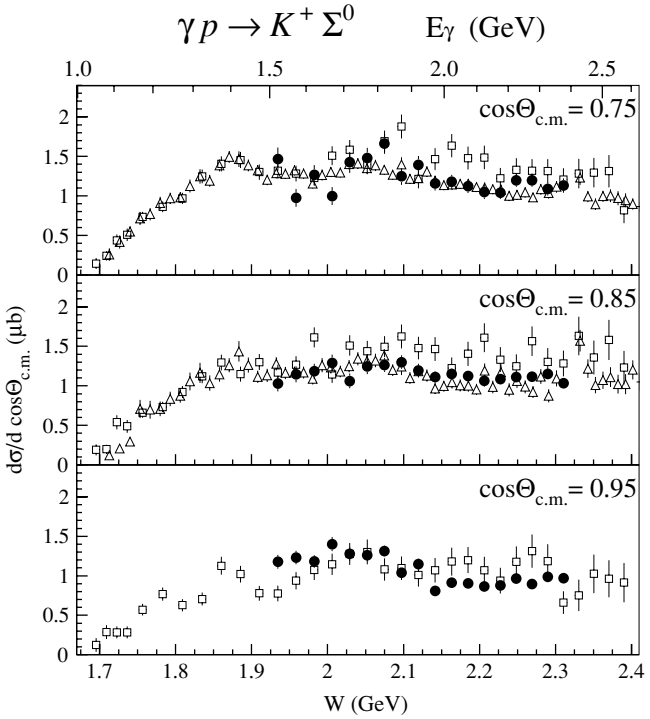

FIG. 14. Energy dependence of differential cross sections for the $\gamma p \to K^+\Sigma^0$ reaction. The closed circles are the results of the present analysis. The open squares and triangles are the data measured by the SAPHIR [3] and the CLAS [10] Collaborations, respectively. Errors are only because of the statistical one.

because of accidental vetoes and δ-ray reactions was measured to be lower than 1.6%.

The results from the SAPHIR Collaboration (square) and the CLAS Collaboration (triangle) are also plotted in Figs. 13 and 14 for comparison. Differential cross sections for the $K^+\Lambda$ reaction gradually decrease as the photon energy increases as shown in Fig. 13. There is the large discrepancy between the CLAS and SAPHIR data at $\cos\Theta_{\text{c.m.}} = 0.75$ and 0.85, and this causes difficulty in simultaneous fitting for theoretical models. It is important to solve these experimental discrepancies to obtain a conclusion for the existence of new resonances.

The LEPS data are in good agreement with the CLAS data within the total uncertainty and are systematically higher than the SAPHIR data at all angles. The difference between the LEPS and the SAPHIR data is small at $\cos\Theta_{\text{c.m.}} = 0.75$ and 0.85 and is significant at $\cos\Theta_{\text{c.m.}} = 0.95$, in particular at $W \sim 1.95$ GeV, where it reaches up to 32%. The LEPS data support the CLAS data rather than the SAPHIR one. A small bump structure is seen at $W \sim 1.96$ GeV in the CLAS and SAPHIR data at $\cos\Theta_{\text{c.m.}} = 0.75$ and 0.85, but the discrepancy in the values is large. The LEPS data show the bump structure at $W \sim 1.96$ GeV and support the CLAS results. At $\cos\Theta_{\text{c.m.}} = 0.95$, the LEPS data still have the bump structure at $W \sim 1.96$ GeV, but no prominent structure is seen in the SAPHIR data. The bump structure in the LEPS data is recognizable even if the sizable total errors (about 7% systematic and 5%–8% statistical) are taken into consideration.

Differential cross sections for the $K^+\Sigma^0$ reaction increase slightly at $W \sim 2.05$ GeV in both the LEPS and CLAS data. The cross sections for the $K^+\Sigma^0$ reaction are about 20% smaller than those for the $K^+\Lambda$ reaction. The LEPS data are about 10% smaller than the SAPHIR data at $W > 2.1$ GeV. At $\cos\Theta_{\text{c.m.}} = 0.95$, the discrepancy between the LEPS and SAPHIR data is large around $W \sim 1.93$ GeV.

V. DISCUSSION

A. Photon-beam asymmetries

The experimental data of photon-beam asymmetries are compared with the results of theoretical calculations in Fig. 15. The models used in the calculations are listed in Table IV. The dot-dashed curves are the results of the Regge model with the K and K^* exchanges by Guidal *et al.* [19]. The dashed curves in the $K^+\Lambda$ reaction are the results of the Gent isobar model by D.G. Ireland *et al.* [7]. The dotted curves in the $K^+\Sigma^0$ reaction are the results of the Gent isobar model by T. Corthals *et al.* [20]. The solid curves are the results of the mixing model of the Feynman diagram and the Regge model by Mart and Bennhold [21].

The results of the Regge model calculation [22] are compared with the data at $W = 2.196$ and 2.280 GeV, where the t-channel contribution is expected to become large. The photon-beam asymmetry is a good means to study meson-exchange in the t channel. The Regge model

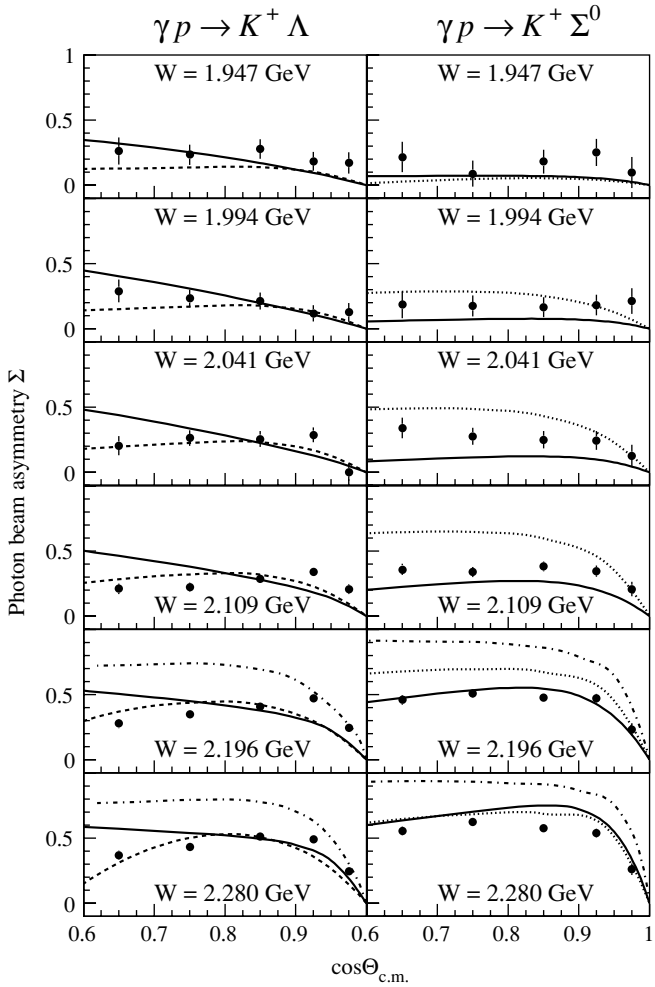

FIG. 15. Photon beam asymmetries for the $\gamma p \to K^+\Lambda$ (left) and $\gamma p \to K^+\Sigma^0$ (right) reactions as a function of $\cos\Theta_{\mathrm{c.m.}}$. The dot-dashed curves are the results of the Regge model with K and K^* exchanges by Guidal *et al.* [19]. The dashed curves in the $K^+\Lambda$ reaction are the results of the Gent isobar model by D.G. Ireland *et al.* [7]. The dotted curves in the $K^+\Sigma^0$ reaction are the results of the Gent isobar model by T. Corthals *et al.* [20]. The solid curves are the results of the mixing model of the Feynman diagram and the Regge model by Mart and Bennhold [21].

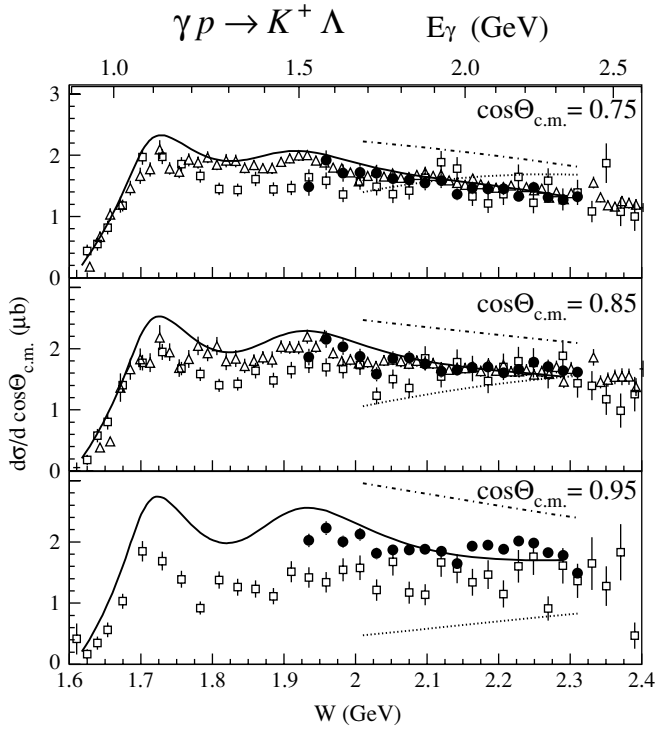

FIG. 16. Energy dependence of differential cross sections for the $\gamma p \to K^+\Lambda$ reaction. The closed circles, open squares, and open triangles are from the LEPS, SAPHIR [3], and CLAS [10], respectively. The dot-dashed and dotted curves are the results of the Regge model with the K and K^* exchanges and the K^* exchange, respectively, obtained by Guidal *et al.* [19]. The solid curves indicate the result of the mixing models of the Feynman diagram and the Regge model [21].

is valid only at forward angles and at high energies, and the s channel contribution seems to be not negligible even at $W = 2.1$–2.3 GeV. Although the Regge model calculation indicates a sharp decrease at forward angles, which the data show, the model overestimates the data in both reactions and the discrepancy between the results of the model calculation and the experimental data becomes large at backward angles.

The Gent isobar-model calculation for the $K^+\Lambda$ reaction agrees with the LEPS data except for a sharp decrease at forward angles. The model calculation for the $K^+\Sigma^0$ reaction overestimates the data at $W = 2.0$–2.2 GeV and mostly agrees with the data at $W < 2.0$ GeV and $W = 2.28$ GeV. The Mart-Bennhold-model calculation for the $K^+\Lambda$ reaction mostly agrees with the data but shows a discrepancy with the data at $\cos\Theta_{\mathrm{c.m.}} < 0.75$ and cannot reproduce the sharp decrease at forward angles. The model calculation for the $K^+\Sigma^0$ reaction mostly agrees with the data.

TABLE IV. List of the theoretical models. The N^* resonances, $S_{11}(1650)$, $P_{11}(1710)$, $P_{13}(1720)$, and $D_{13}(1900)$ are for the $K^+\Lambda$ and $K^+\Sigma^0$ reactions. The Δ^* resonances, $S_{31}(1900)$ and $P_{31}(1910)$, are for the $K^+\Sigma^0$ reaction only. In the Gent model calculation, $\Lambda(1800)$ and $\Lambda(1810)$ resonances are for the $K^+\Lambda$ reaction, and $\Lambda(1810)$ and $\Lambda(1880)$ are for the $K^+\Sigma^0$ reaction.

Name	Model	t channel	s channel	u channel
Guidal [22]	Regge	K, K^*	None	None
Gent group [7,8,20]	Isobar	K, K^*, K_1	S_{11}, P_{11}, P_{13}, D_{13}, S_{31}, P_{31}	$\Lambda(1800)$, $\Lambda(1810)$, $\Lambda(1880)$
Mart-Bennhold [21]	Isobar+Regge	K, K^*, K_1	S_{11}, P_{11}, P_{13}, D_{13}, S_{31}, P_{31}	None

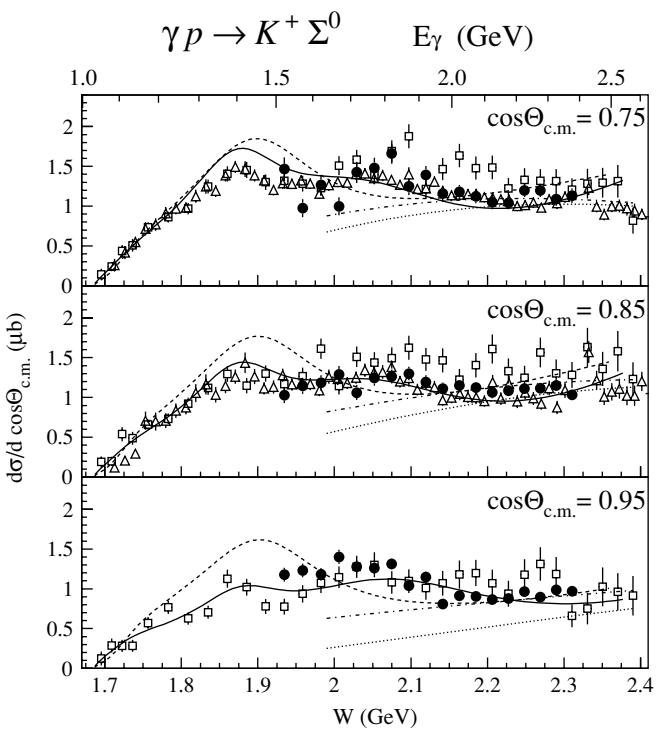

FIG. 17. Energy dependence of differential cross sections for the $\gamma p \to K^+\Sigma^0$ reaction. The closed circles, open squares, and open triangles are from the LEPS, SAPHIR [3], and CLAS [10], respectively. Dot-dashed and dotted curves are the result of the Regge model with the K and K^* exchanges and the K^* exchange, respectively, obtained by Guidal *et al.* [19]. Solid curves indicate the result of the mixing models of Feynman diagram and Regge model [21]. Dashed curves are the model calculation by the Gent group [20].

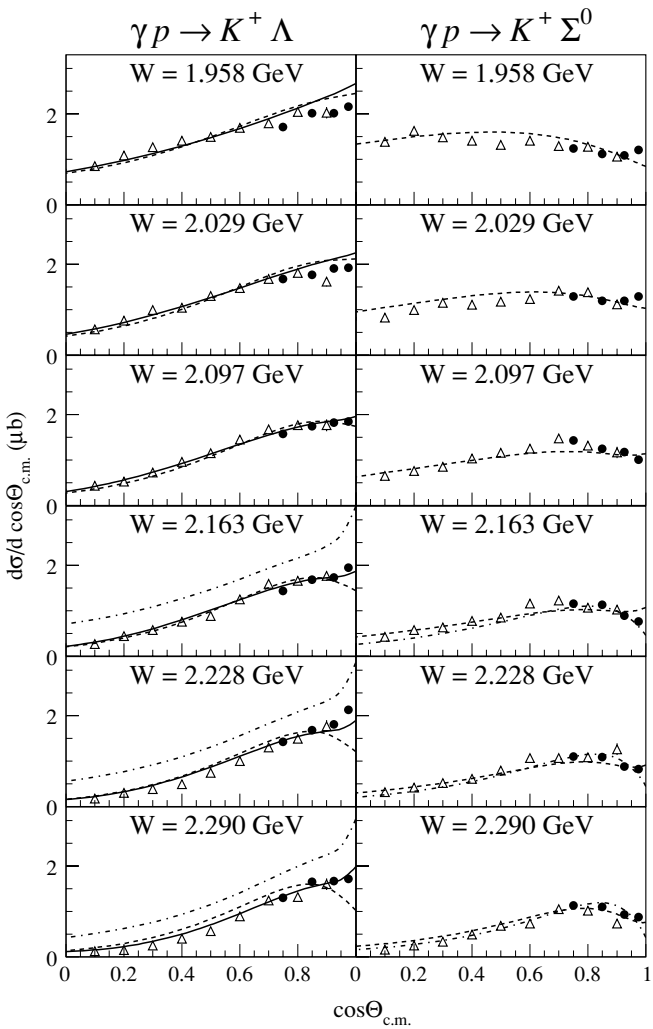

FIG. 18. Angular dependence of differential cross sections for the $\gamma p \to K^+\Lambda$ (left) and $\gamma p \to K^+\Sigma^0$ (right) reactions. Closed circles are LEPS data and open triangles are CLAS data. Dot-dashed, dashed, and solid curves are the theoretical calculations with the Regge model, the Feynman diagram, and the mixing model of the Regge model and the Feynman diagram, respectively [21].

B. Differential cross sections

The differential cross sections for the $K^+\Lambda$ reaction are shown as a function of the total energy comparing with theoretical calculations in Fig. 16. Mart and Bennhold's model calculation shows a good agreement with the LEPS and the CLAS data in all ranges. The resonance-like structure at $W = 1.96$ GeV is well reproduced by including the missing resonance $D_{13}(1900)$. The Gent model calculation also include the $D_{13}(1900)$ resonance to reproduce the resonance-like structure [7,8]. The K and K^* exchanges model calculation of the Regge theory overestimates the data, whereas the K^* exchange model underestimates data at forward angles. The difference between the K and K^* exchanges model, compared with the K^* exchange only model, becomes large at forward angles because K exchange is dominant at forward angles and makes a forward peak for the $K^+\Lambda$ reaction in the Regge model.

The differential cross sections for the $K^+\Sigma^0$ reaction are shown as a function of the total energy with the results of the theoretical calculations in Fig. 17. The K and K^* exchange model underestimates the data at $W < 2.15$ GeV but shows an agreement at $W > 2.15$ GeV where the t-channel contribution is expected to be dominant. In the Regge model, the contribution of the K exchange for the $K^+\Sigma^0$ reaction is smaller than that for the $K^+\Lambda$ reaction because the coupling constant $|g_{K\Sigma N}|$ is smaller than $|g_{K\Lambda N}|$ [15]. The difference between the Regge models using K and K^* exchanges, compared with the model having only K^* exchange, is smaller than that for the $K^+\Lambda$ reaction.

A small enhancement is seen at $W = 2.05$ GeV. The total systematic error is about 7% and the statistical error is 6 to 8% at the enhancement. The enhancement in the data is within the total errors and is not well reproduced by models without resonances. The CLAS data show a small enhancement at $W =$ 2.05 GeV [10]. A similar structure could be seen in the LEPS data, despite the fact that it is not statistically significant (the systematic error being about 7% and statistical 6%–8% at the enhancement). The Gent isobar-model calculation does not introduce a resonance at this region and underestimates the

experimental data. Large predicted photon-beam asymmetries compared with the experimental data may be explained by the absence of a resonance in the calculation. However, in the Mart-Bennhold's model calculation the $P_{31}(1910)$ Δ resonance moves to $W = 2.05$ GeV, and the measured differential cross sections are reasonably reproduced in this energy region. The Δ^* resonance strongly couples to the $K^+\Sigma^0$ channel, and a Δ^* resonance seems to be required to explain the enhancement at $W = 2.05$ GeV.

The differential cross sections are shown as a function of the K^+ scattering angle in Fig. 18. The LEPS data connect smoothly to the CLAS data. It is seen that the $K^+\Lambda$ cross section increases at forward angles, whereas the $K^+\Sigma^0$ cross section decreases except for the low-energy regions of $W =$ 1.947 and 2.029 GeV. The experimental data for the $K^+\Lambda$ and $K^+\Sigma^0$ reactions are compared with Mart and Bennhold's model calculation in Fig. 18.

The mixing model calculation agrees with the data for the $K^+\Lambda$ reaction, whereas the calculation of the Feynman diagram agrees only with the data for the $K^+\Sigma^0$ reaction. The calculations of the Feynman diagram increase as the scattering angle becomes smaller, then they drop at $\cos\Theta_{\text{c.m.}} > 0.85$ for both reactions. The model calculation without inclusion of Regge amplitudes cannot explain the observed angular distributions for the $K^+\Lambda$ reaction. The Regge model calculation shows steep increase for the $K^+\Lambda$, whereas it drops for the $K^+\Sigma^0$ at $\cos\Theta_{\text{c.m.}} > 0.9$. In the Regge model, the K exchange contribution is large for the $K^+\Lambda$ but is small for the $K^+\Sigma^0$ at forward angles. In the high energy data measured at $W >$ 3.2 GeV at SLAC, the $K^+\Lambda$ shows a forward peak but the $K^+\Sigma^0$ does not [23]. This result was discussed in terms of the dominance of the K exchange for the $K^+\Lambda$ [15]. In our data the same feature is seen at $W = 2.1$ to 2.3 GeV. The mixing model, which includes the Regge model with a dominant K exchange contribution, reproduces well the differential cross sections for the $K^+\Lambda$ reaction.

VI. SUMMARY

The photon-beam asymmetries and differential cross sections for the $\gamma p \to K^+\Lambda$ and $\gamma p \to K^+\Sigma^0$ reactions have been measured at $E_\gamma = 1.5$–2.4 GeV and at $0.6 < \cos\Theta_{\text{c.m.}} < 1$ by using linearly polarized photons at the SPring-8/LEPS facility. The photon-beam asymmetry data for the $\gamma p \to K^+\Lambda$ and $\gamma p \to K^+\Sigma^0$ reactions have been obtained for the first time in this energy range. The sign of the photon beam asymmetry has been found to be positive.

We obtained differential cross sections with good statistics at forward angles. The present data of the differential cross sections are consistent with those obtained by the CLAS Collaboration in the overlapping region. The differences of these two data are within the expected error. The resonance structure at $W = 1.96$ GeV is seen in the $\gamma p \to K^+\Lambda$ reaction and this is expected to be the same structure as one found in the SAPHIR and CLAS data. This bump structure can be explained by including a $D_{13}(1900)$ resonance. A small enhancement has been found at $W = 2.05$ GeV in the $\gamma p \to K^+\Sigma^0$ reaction and the structure is partly reproduced by including the P_{31} Δ^* resonance. The differential cross sections for the $\gamma p \to K^+\Lambda$ reaction rise at forward angles, whereas the cross sections for the $\gamma p \to K^+\Sigma^0$ reaction drop. This forward peak in the $K^+\Lambda$ channel comes from the large contribution of K exchange in the t channel. Our data indicate that K exchange is dominant in the $\gamma p \to K^+\Lambda$ reaction but not dominant in the $\gamma p \to K^+\Sigma^0$ reaction.

ACKNOWLEDGMENTS

We thank the staff at SPring-8 for providing excellent experimental conditions during the long experiment. This research was supported in part by the Ministry of Education, Science, Sports and Culture of Japan, by the National Science Council of the Republic of China (Taiwan), and by the National Science Foundation (USA).

[1] S. Capstick and W. Roberts, Phys. Rev. D **49**, 4570 (1994).
[2] S. Capstick and W. Roberts, Phys. Rev. D **58**, 074011 (1998).
[3] M. Q. Tran *et al.* (SAPHIR Collaboration), Phys. Lett. **B445**, 20 (1998).
[4] T. Mart and C. Bennhold, Phys. Rev. C **61**, 012201(R) (1999).
[5] T. Mart, C. Bennhold, H. Haberzettl, and L. Tiator, *KaonMAID 2000* at http://www.kph.uni-mainz.de/MAID/kaon/kaonmaid.html
[6] S. Janssen, J. Ryckebusch, D. Debruyne, and T. Van Cauteren, Phys. Rev. C **65**, 015201 (2001).
[7] D. G. Ireland, S. Janssen, and J. Ryckebusch, Nucl. Phys. **A740**, 147 (2004).
[8] S. Janssen, J. Ryckebusch, D. Debruyne, and T. Van Cauteren, Phys. Rev. C **66**, 035202 (2001).
[9] B. Saghai, *International Symposium on Hadrons and Nuclei, Seoul, Korea* (2001).
[10] J. W. C. McNabb *et al.* (CLAS Collaboration), Phys. Rev. C **69**, 042201 (2004); R. Bradford *et al.* (CLAS Collaboration), *ibid.*, in print and nucl-ex/0509033.
[11] K. H. Glander *et al.*, Eur. Phys. J. A **19**, 251 (2004).
[12] R. G. T. Zegers, M. Sumihama *et al.* (LEPS Collaboration), Phys. Rev. Lett. **91**, 092001 (2003).
[13] D. S. Carman *et al.* (CLAS Collaboration), Phys. Rev. Lett. **90**, 131804 (2003).
[14] P. Stichel, Z. Phys. **180**, 170 (1964).
[15] M. Guidal, M. Laget, and M. Vanderhaeghen, Nucl. Phys. **A627**, 645 (1997).
[16] A. D'Angelo, O. Bartalini, V. Bellini, P. Levi Sandri, D. Moricciani, L. Nicoletti, and A. Zucchiatti, Nucl. Instrum. Methods A **455**, 1 (2000).
[17] R. Frühwirth, Nucl. Instrum. Methods A **262**, 444 (1987).
[18] J. P. Bocquet *et al.*, Nucl. Phys. **A691**, 466c (2001).
[19] M. Guidal, J.-M. Laget, and M. Vanderhaeghen, Phys. Rev. C **68**, 058201(R) (2003).
[20] T. Corthals, private communication.
[21] T. Mart and C. Bennhold, *Kaon Photoproduction in the Feynman and Regge Theories*, arXiv:nucl-th/0412097.
[22] M. Guidal, private communication.
[23] A. M. Boyarski, F. Bulos, W. Busza, R. Diebold, S. D. Ecklund, G. E. Fischer, Y. Murata, J. R. Rees, B. Richter, and W. S. C. Williams, Phys. Rev. Lett. **22**, 1131 (1969).